Renewable Energy 235 (2024) 121275

Contents lists available at ScienceDirect

Renewable Energy

journal homepage: www.elsevier.com/locate/renene

Design, simulation and on-sun experiments of a modified sliding-bed particle solar receiver for coupling with tower concentrating system

Xiangyu Xie [a,b], Peiwang Zhu [a,b,c,**], Mingjiang Ni [a,b,c], Fengyuan Chai [a,b], Jiasong Li [a,b], Gang Xiao [a,b,c,*]

[a] Key Laboratory of Clean Energy and Carbon Neutrality of Zhejiang Province, Zhejiang University, 38 Zheda Road, Hangzhou, Zhejiang, 310027, China
[b] State Key Laboratory of Clean Energy Utilization, Zhejiang University, 38 Zheda Road, Hangzhou, 310027, China
[c] Jiaxing Research Institute, Zhejiang University, 1300 Dongshengxilu Road, Jiaxing, 314031, China

ARTICLE INFO

Keywords:
Solar radiation
Sliding-bed particle receiver
Structural design
On-sun experiments

ABSTRACT

A modified sliding-bed particle solar receiver was proposed to realize the coupling with upward concentrating system, which was a challenge for the previous designs. The newly added secondary reflection structure could not only adjust the optical path, but also preheated the particles flowing behind it. The overall principle of the receiver, the regulation mechanism of the particle layer thickness and the control and measurement method of the particle flowrate have all been described in detail. After the cold-state research on flow pattern, on-sun experiments based on a tower concentrating system were conducted to evaluate the receiver performance. Experimental results showed that the maximum outlet temperature of ~860°C and single-pass temperature rise of ~510°C were achieved. Under various DNI and time, the average outlet temperature ranging from ~535 °C to 782 °C, and positive efficiency ranging from ~51 % to 66 % were obtained. A concentrating-receiving coupled model was proposed to analyze the energy transfer process during the experiments, and to predict the receiver performance under higher incident power. Simulation results showed that the thermal loss rate could be reduced from 28.48 % to 13.22 % with 5 times magnification of the incident power, but the local overheating risk of the secondary reflective surface required attention.

1. Introduction

The effective utilization of solar radiation has the potential to alleviate the increasingly severe energy and environmental problems in the world. Compared to water/steam, molten salt, etc, using particle as the heat transfer medium (HTM) of concentrating solar power (CSP) systems has the potential to achieve higher temperature, better stability, and better temperature adaptability [1–4]. Particle solar receiver (PSR) is the component that converts solar radiation into the thermal energy within particle, and is one of the most challenging components to design in CSP, as it must directly withstand fluctuating, uneven, and highly concentrated solar radiation. Various concepts and designs of particle solar receivers have been proposed since 1980s [5], and many tests and improvements have been conducted thereafter. The core of the design of PSR lies in the realization form of the transfer and heating of the particles under extreme high-temperature and high-flux conditions. For a better understanding of the PSR concept and design proposed in this article, the following will summarize the design core of some typical PSRs.

According to whether particles absorb solar radiation directly, PSRs can be divided into indirect and direct types. For indirect types, outer walls such as stainless steel tubes [6] are firstly heated by the solar radiation, and then transfer the thermal energy to the particles flowing behind. Typical indirect PSRs include: dense suspension PSR which uses fluidizing gas to drive a dense suspension of particles to move upward in vertical absorbing tubes [6–8], particle-filled PSR which allows particles to flow downward in vertical absorbing tubes by gravity [9], counterflow fluidized bed PSR which allows particles to flow downward in fluidized bed by gravity while using upward fluidizing gas to enhance heat transfer coefficient [10,11], near-blackbody enclosed PSR which

* Corresponding author. Key Laboratory of Clean Energy and Carbon Neutrality of Zhejiang Province, Zhejiang University, 38 Zheda Road, Hangzhou, Zhejiang, 310027, China.
** Corresponding author. Key Laboratory of Clean Energy and Carbon Neutrality of Zhejiang Province, Zhejiang University, 38 Zheda Road, Hangzhou, Zhejiang, 310027, China.
E-mail addresses: zhupw@zju.edu.cn (P. Zhu), xiaogangtianmen@zju.edu.cn (G. Xiao).

https://doi.org/10.1016/j.renene.2024.121275
Received 3 February 2024; Received in revised form 23 August 2024; Accepted 30 August 2024
Available online 31 August 2024
0960-1481/

allows particles to flow downward between absorbing tubes array by gravity while homogenizing the distribution of incident power by multiple reflection [12,13] and etc. Indirect PSRs usually have better control over the particle transfer, less possibility to cause particle leakage, and almost no requirements on the particle absorptivity. But due to the poor thermal conductivity of particles, indirect PSRs typically have lower heat transfer efficiency and lower allowable peak flux density [2], thus facing greater overheating risk. In addition, the high flux, high fluctuation, and non-uniformity of concentrated solar radiation places extremely high demands on the materials of outer walls. For direct types, the solar radiation directly heats the particles. Typical direct PSRs include: falling PSR which allows particles to fall in the form of a curtain by gravity [5,14], obstructed falling PSR which allows particles to fall through chevron-shaped mesh structures to reduce the falling velocity and improve the temperature rise [15–18], multi-stage falling PSR which allows particle curtain to be repeatedly initialized by using intermediate troughs to enhance the hydrodynamic stability and improve the radiation absorption [19–25], centrifugal PSR which allows particles to slide down along the internal walls of a cylindrical cavity by gravity, while adjusting sliding speed by centrifugal force [26–28], quartz tube PSR which allows particles to flow downward in transparent quartz tubes by gravity [29–31], spiral PSR which uses the vibration of spiral surface to drive particles to move upward along a spiral path [32,33], autothermal fluidized bed PSR which allows particles to flow upward to the direct radiation zones due to the pressure difference [34,35], sliding-bed PSR which allows particles to slide downward along an inclined plate in the form of a sliding-bed by gravity [36–38] and etc. Compared to indirect types, direct PSRs usually have higher solar receiving efficiency due to the direct absorption of solar radiation by particles, and have higher limit of incident power, temperature, and adaptability due to the real-time removal of the concentrated solar radiation through particle mass flow. However, since direct PSRs are typically open systems, it is challenging to utilize methods such as fluidizing gas to drive particle movement and to employ clear boundary constraints on particles. Therefore, direct PSRs usually have relatively poor control on particle transfer, higher risk in particle leakage, and higher requirements for particle absorptivity. Quartz tube PSR is a unique direct PSR type which uses quartz tubes to form a closed system to alleviate some of the problems mentioned above, but there are still challenges in terms of fragility, susceptibility to contaminating, and manufacturing difficulties associated with quartz tubes.

For sliding-bed PSR, one of the direct PSRs, good performance in particle flowrate control and single-pass temperature rise was reported. However, due to the interception of upward incident rays by the inclined plane itself, common sliding-bed PSR are more suitable for downward concentrating systems, but difficult to adapt to upward concentrating systems such as a tower concentrating system.

In this paper, a modified sliding-bed particle solar receiver with an internal secondary reflection structure was proposed to address the aforementioned problem, which further enhances the versatility and scalability potential. The secondary reflection structure in the modified PSR, which was much like the outer walls of indirect PSRs, played two roles at the same time: reflecting the incident rays to the particles flowing on the solar absorbing slope, and preheating the particles flowing inside the preheating channel. The former realized the coupling with upward concentrating systems, while the latter further utilized the incident power and thereby improved the receiving efficiency. The solar absorbing slope in the modified PSR was basically the same as that of the common PSR, which could preserve the original advantage such as higher single-pass temperature rise [36]. Currently, the specific structural design of the receiver was demonstrated and implemented. Some preliminary research on cold-state flow pattern was conducted to ensure the safe operation of the receiver. Some on-sun experiments were conducted to evaluate the temperature and efficiency performance of the receiver. A concentrating-receiving coupled model was proposed to analyze the specific heat transfer process and heat loss composition of the on-sun experiments, as well as to predict the changes in efficiency and risk under higher incident power.

Nomenclature

Latin letters		**Abbreviations**	
A	area	CSP	concentrating solar power
c	specific heat	*DNI*	direct normal irradiance
d	distance	FR	flowrate
d	layer or interlayer thickness	HB	baffle height
e	energy	HTM	heat transfer medium
Gr	Grashof number	PSR	particle solar receiver
g	gravity coefficient	SSPSR	sliding-bed PSR with secondary reflection
h	convection coefficient		
l	(characteristic) length		
lg	intermediate gap in length	**Subscripts**	
$\dot{m}$	mass flowrate	a	air
$\vec{n}$	normal direction	a	aiming point
n	number	ap	aperture
O	centre position	ave	average property
$\overrightarrow{out}$	reflected direction of ray	$conv$	convection
p	position	$cond$	conduction
Pr	Prandtl number	e	emission
Q	power	$flow$	particle flow
R	random number between 0 and 1	h	heliostat
r	radius	hf	heliostat field
$\vec{r}$	reflection direction	i	insulation
$\vec{s}$	ray direction	inc	incident
T	temperature	$inner$	inner objects of receiver
T_m	characteristic temperature	in	inlet
u	unit vector	n	negative
		out	outlet
Greek letters		opt	optical property
α	flow angle	p	positive
α	altitude angle	p	particles
θ	zenith angle	r	secondary reflective surface
φ	azimuth angle	r	reflection
φ	loss rate	rad	radiation
η	(atmospheric attenuation) factor	ray	ray
η	efficiency	s	stainless steel
ε	emissivity	s	sun
ρ	reflectivity	sum	sum property
λ	thermal conductivity	t	target
υ	kinematic viscosity coefficient	$ther$	thermal property
ρ	bulk density	x	vector in x-axis
τ	time step	y	vector in y-axis
σ	Stefan-Boltzmann constant	z	vector in z-axis

2. Receiver design

2.1. Overall principle

The particles as the HTM of the receiver were a type of sintered bauxite, which was commonly used as a proppant in oil fracturing. The physical properties of the particles are listed in Table 1.

The overall structure of the receiver is shown in Fig. 1, which consists

Table 1
Physical properties of the particles (sintered bauxite).

Physical properties	Item
Composition	83%Al_2O_3, 5%SiO_2, 6%Fe_2O_3 and others
Size (mm)	0.5–0.8 (average ~0.712)
Absorptivity	~85 %
Heat capacity (J/(kg*K))	756 (25 °C)-1275 (700 °C)
Bulk density (kg/m^3)	1800
Density (kg/m^3)	2650
Packing limit	0.68
repose angle	23.5°
thermal conductivity (W/(m*K))	0.23(20 °C)-0.54(800 °C)

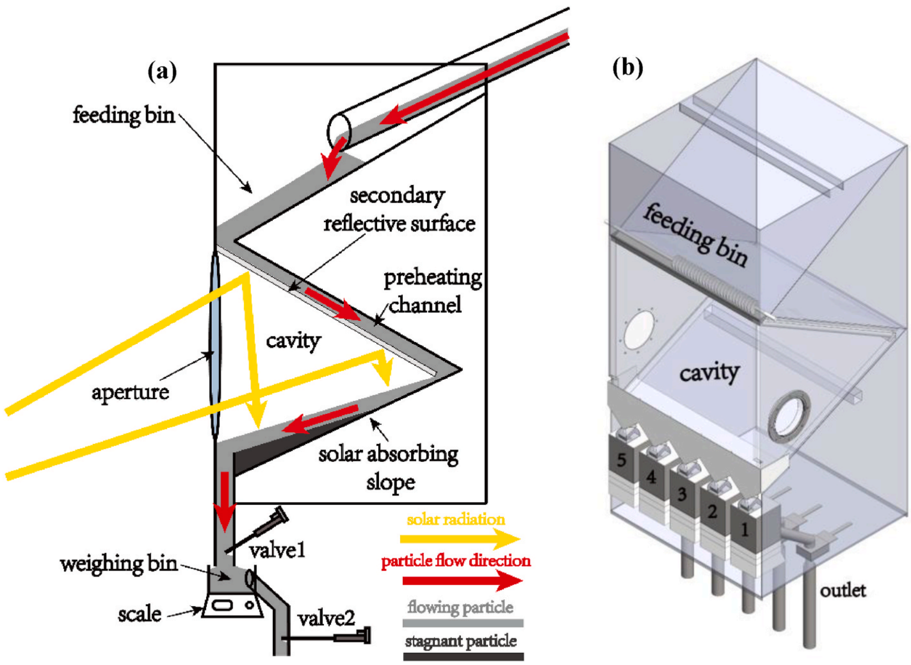

Fig. 1. Schematic dia gram (a) and structural drawing (b) of a SSPSR.

of one feeding bin, one preheating channel, one solar receiving cavity (including one reflective surface and one solar absorbing slope), multiple flowrate measurement and control devices, and multiple discharge outlets. Based on the flow process of particles, the function and design logic of each component in the receiver will be introduced in order. The particles entering from the inlet of the receiver will be temporarily stored in the feeding bin, and then enter the preheating channel. The preheating channel closely adheres to the secondary reflective surface. The secondary reflective surface is composed of materials with high reflectivity. Most of the incident rays are reflected, while the rest of the incident rays are absorbed and transmitted by the secondary reflective surface. The absorbed and transmitted incident rays are converted into the thermal power inside the secondary reflective surface and preheating channel, and then are transferred to the particles flowing in the preheating channel through conduction. The particles leaving the preheating channel will flow into the solar absorbing slope and then directly absorb the rays reflected by the secondary reflective surface. The secondary reflective surface and the preheating channel together form a receiving structure similar to a particle-filled PSR with outer walls [9], while the difference between the secondary reflective surface and the outer walls lies in the function. The former is for reflection, while the latter is for absorption. Obviously, the former has a better potential for higher allowable peak flux density. After being indirectly preheated and directly radiated, particles will cross an end baffle, pass through a connecting funnel and then be controlled by a gate valve. The weighing device beneath the valve measures the real-time particle flowrate. Finally, the particles will exit the receiver and enter the subsequent component of the CSP system, such as a high-temperature storage bin.

In current design, the receiver has five sets of gate valves and connecting funnels along the transverse direction, which thereby divides the solar absorbing slope and preheating channel into five relatively independent parts. Facing the receiver from the outside of the aperture, the rightmost area is defined as the 1st part, and the leftmost area is defined as the 5th part. The transverse partitioning facilitates the custom control of particle flow, and the specific principles and effects are to be elaborated in subsequent sections.

2.2. Regulation mechanism of the particle layer thickness

For the particle layer sliding on the solar absorbing slope, the thickness directly affects the average temperature. In application, To ensure the flow stability, the inclination angle β of the solar absorbing slope should be at least $1 \sim 2^{\circ}$ greater than the flow angle α of particle as shown in Fig. 2. Therefore, as the particles flowing downward, the thickness of the particle layer gradually increases from d_1 to d_2, which results in a lower average temperature at the end of the particle layer. The baffle arranged at the end of the slope with a height of d_3 can divide the particle layer into two parts: flowing particle layer and stagnant particle layer. As a result, the thickness of the particle layer upon leaving the slope decreases from d_2 to d_2', which reduces the temperature drop along the depth direction and increase the average particle temperature. Meanwhile, the stagnant particle layer serves as a thermal insulation to protect the slope below.

Due to manufacturing and installation errors, as well as thermal deformation, there are often differences in the thickness of the particle layer along the transverse direction. To ensure the suitable particle layer thickness at different positions as much as possible, five baffles with different heights were arranged at the end of the solar absorbing slope. Specifically, due to thermal deformation, the center of the slope end was slightly concave, requiring the highest intermediate baffle. The overall receiver was slightly tilted to the right, so the right baffles were slightly higher than the left ones.

2.3. Control and measurement method of the particle flowrate

A gate valve was specially designed to control the flowrate of high-temperature particles and thereby addressed the high fluctuation of incident solar radiation. Five gate valves were arranged in the transverse direction to achieve the adjustment of the particle flowrate distribution and thereby addressed the non-uniformity of the incident solar radiation. The gate valve's fundamental structure is illustrated in Fig. 3. The key to the gate valve design lies in resolving the contradiction between thermal expansion allowance and particle sealing, while the arrangement of stacking plate and the oblique placement of the valve solve the above contradiction. The specific design detail can be obtained in supplementary material.

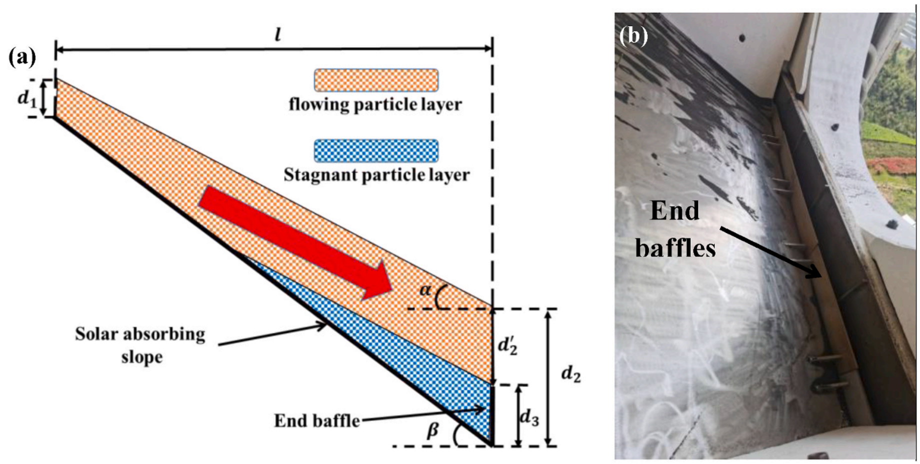

Fig. 2. Schematic diagram of the effect of end baffle(a) and the baffles arranged at the end of the slope(b).

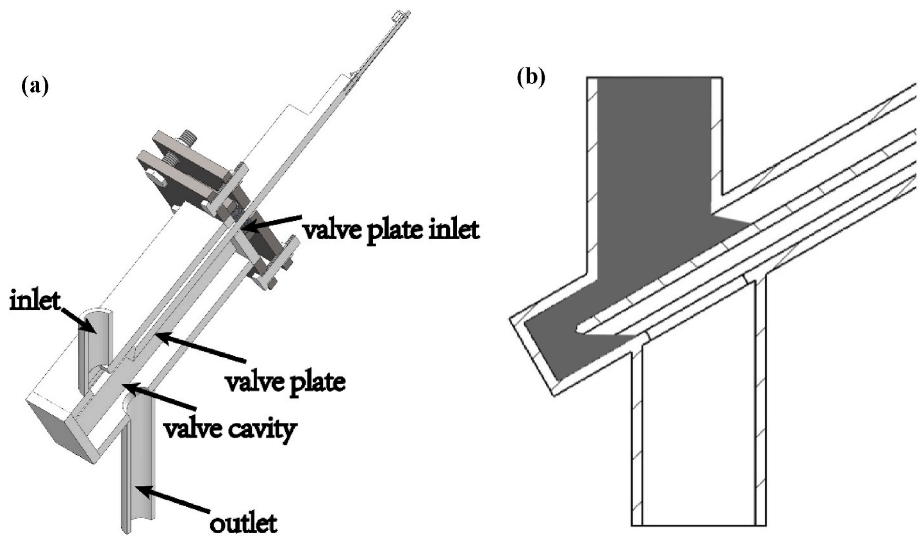

Fig. 3. Structural drawing of the gate valve(a) and schematic diagram of valve shutdown state (b).

To better adjust the particle flow and facilitate subsequent computational analysis, it is imperative to the measure the specific real-time flowrate for high-temperature particles. Unlike conventional fluids such as water, air and etc, there are very few mature commercial devices for measuring the flowrate of particles, especially at a high temperature exceeding 800 °C. Herein, a specific setup and methodology was

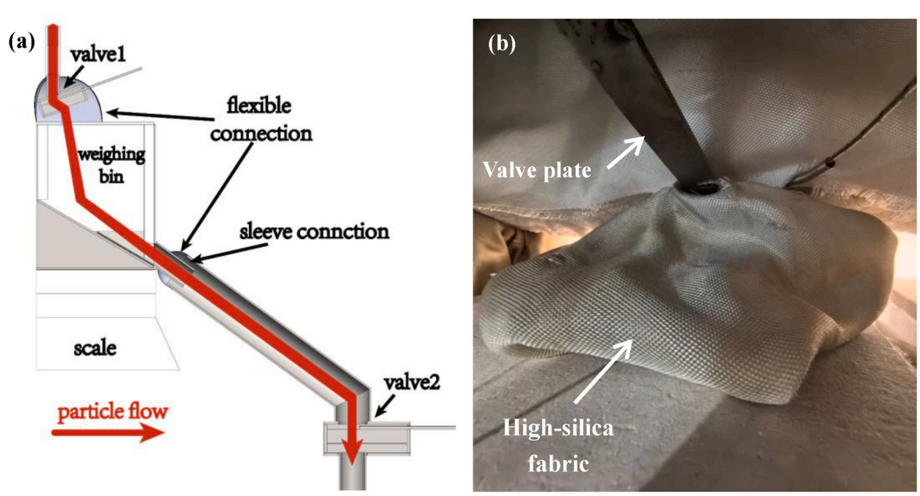

Fig. 4. Structural drawing of the flowrate measurement setup(a) and flexible connection between valve and weighing bin (b).

designed to achieve the measurement through the collaboration of one weighing bin, one scale and two valves as shown in Fig. 4(a). When valve2 is closed, the particles leaving valve1 will enter the weighing bin for temporary storage. The scale below will measure the total weight of the weighing bin and the internal particles in real time. The particle flowrate can be obtained by calculating the ratio of weight change to time change. When the weighing bin is about to be full, valve2 will open to unload the particles until the weight of particles in the weighing bin reaches a certain lower limit, and then valve2 will close and the flowrate measurement and calculation process described above will be repeated.

In order to achieve the accurate weight measurement, the weighing bin needs to be independently arranged, which indicates that the weighing bin should not be affected by the force given by other components. However, if the weighing bin is not in contact with other components, it is prone to cause particle leakage and heat loss at the inlet and outlet. The use of sleeve connection and flexible connection alleviates the above problems. As shown in Fig. 4(a), since particles can only move downward by gravity, extending the outlet pipe of the weighing bin into a certain depth inside the subsequent pipe, i.e. sleeve connection, can avoid the contact between the pipes, while still enabling particle transport. The core material of the flexible connection is high-silica fabric, an inorganic cloth with high temperature resistance and high thermal insulation. The high-silica fabric is soft in texture. According to cold-state tests, when the high-silica fabric was connected in a relaxed state as shown in Fig. 4(b), it barely affected the accuracy of the weighing. According to on-sun tests, when the particles over 800 °C flowed through the inlet and outlet of the weighing bin, the application of 0.5 mm high-silica fabric in these areas could reduce the external temperature to below 100 °C. In addition, due to the hot-air sealing effect and the high reflectivity (~80 %) of high-silica fabric, the convection and radiation loss were further reduced.

3. Model

A concentrating-receiving coupled model for heliostat field and receiver was proposed. Monte Carlo method was used in ray tracing to model stochastic physical events such as ray emission, absorption, transmission and reflection on the surface of various objects. An optical-thermal coupled model discretizing the heat transfer process in time and space was applied inside the receiver. The significance of the model lies in analyzing the data which are difficult to obtain in experiments, such as the heat loss by ray escaping, and predicting the receiver performance under the conditions which are not currently available, such as multiple times the experimental incident power.

3.1. Concentrating model

The concentrating model is composed of the model of sun, heliostat field and aperture. The sun is the source of rays. The heliostats reflect the rays to the aperture. The aperture receives the rays.

3.1.1. Sun model

The algorithms of sun position have been widely published [39]. The specific calculation procedure of sun position used in this article mainly refers to the instruction manual of a commercial software called soltrace [40] and thereby will not be repeated here. Left-hand coordinate system [O; East-South-Height] is applied in the sun model.

After obtaining the solar altitude angle (α_s) and the solar azimuth angle (φ_s), which are defined as the angle between ray and ground, and the angle between the projection of ray on the ground and the east (positive in clockwise), the preliminary incident direction of ray ($\overrightarrow{s}^*$) can be given as

$$\overrightarrow{s}^* = -[\cos\alpha_s \cos\varphi_s, \cos\alpha_s \sin\varphi_s, \sin\alpha_s] \tag{1}$$

Where the negative sign before the matrix indicates that the ray direction points to the ground.

Local left-hand coordinate systems with $\overrightarrow{s}^*$ as the positive direction of z-axis need to be established, and then the positive unit vector of x-axis (u'_{sx}), y-axis (u'_{sy}) and z-axis (u'_{sz}) can be expressed in Eqs. (2)–(5).

$$u'_{sz} = \overrightarrow{s}^* / |\overrightarrow{s}^*| \tag{2}$$

$$u'_{sx} = [u'_{sz}[2], -u'_{sz}[1], 0] / |[u'_{sz}[1], -u'_{sz}[2], 0]| \tag{3}$$

$$u'_{sy} = u'_{sz} \times u'_{sx} \tag{4}$$

When $u'_{sz}[1] = u'_{sz}[2] = 0$, the u'_{sx} in Eq. (3) should be replaced with Eq. (5)

$$u'_{sx} = [1, 0, 0] \tag{5}$$

Due to the volume of the sun and the distance between the sun and the earth, the core region of the sun is equivalent to a disc with the field angle of ~9.3 mrad to the ground. Using the pillbox model [41] to simulate the angular intensity distribution of rays across the sun's disk, the direction of the incident ray should be uniformly distributed within the field angle. Therefore, the real incident direction of ray ($\overrightarrow{s}$) can be given in Eqs. (6) and (7).

$$\overrightarrow{s}' = [\sin(d\theta'_s)\cos(d\varphi'_s), \sin(d\theta'_s)\sin(d\varphi'_s), \cos(d\theta'_s)] \tag{6}$$

$$\overrightarrow{s} = \overrightarrow{s}' * [u'_{sx}; u'_{sy}; u'_{sz}] \tag{7}$$

Here, $d\theta'_s$, $d\varphi'_s$ and $\overrightarrow{s}'$ are respectively the zenith angle deviation, the azimuth angle deviation and the incident ray direction in the local left-hand coordinate system, where $d\theta'_s$ and $d\varphi'_n$ obeys uniform distribution between $0 \sim 0.0093/2$ and $0 \sim 2\pi$.

In addition, the sky can be simulated by a large enough plane, where the emission positions (p_e) of rays are randomly generated.

3.1.2. Heliostat field model

Coordinate system with normal direction of aperture ($\overrightarrow{n}_{ap}$) as the y-axis positive direction is applied in the heliostat field model to simplify the subsequent calculation as shown in Fig. 5(a). Therefore, a new $\overrightarrow{s}$ should be calculated through a coordinate transformation as shown in Eq. (8).

$$\overrightarrow{s} = \overrightarrow{s} / [u'_{hfx}; u'_{hfy}; u'_{hfz}] \tag{8}$$

Here, u'_{hfx}, u'_{hfy} and u'_{hfz} are respectively the positive unit vector of x-axis, y-axis and z-axis of the heliostat field coordinate system relative to the sun model coordinate system, which can be obtained in a similar way of u'_{sx}, u'_{sy} and u'_{sz}.

Each heliostat has a spherical surface and is composed of four separate mirrors as shown in Fig. 5(b). The radiuses of the heliostat vary from 74 m to 140 m according to the distance between the heliostat and the tower.

The sphere centre (O_h) of each heliostat can be calculated by Eqs. (9) and (10).

$$\overrightarrow{out} = (p_a - p_h) / |p_a - p_h| \tag{9}$$

$$O_h = p_h + \left(\overrightarrow{out} - \overrightarrow{s^*}\right) / \left|\overrightarrow{out} - \overrightarrow{s^*}\right| * r_h \tag{10}$$

Here, $\overrightarrow{out}$ is the reflected direction of ray, p_h and p_a are the position of the heliostat and the aiming point, and r_h is the radius of the heliostat surface.

The reflection position (p_r) of each ray can be obtained by the emission position (p_e), the incident direction ($\overrightarrow{s}$) and the heliostat surface equation as shown in Eqs. (11)–(14).

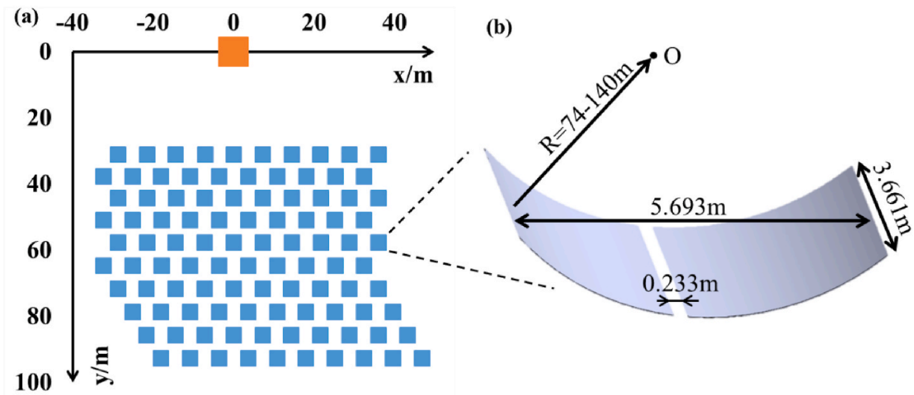

Fig. 5. Configuration and coordinate system of the heliostat field (a) and the shape and size of each heliostat (b).

$$p_r = p_e + \vec{s} * d_{ray} \tag{11}$$

$$|p_r - O_h| = r_h \tag{12}$$

$$p_r' = (p_r - p_h) \Big/ \left[u_{hx}'; u_{hy}'; u_{hz}'\right] \tag{13}$$

$$lg_h \le \left|p_r'[1]\right| \le l_h \ \& \ \left|p_r'[2]\right| \le w_h \ \& \ p_r'[3] \le r_h \tag{14}$$

Here, d_{ray} is the travel distance of ray from sun to heliostat, l_h, lg_h and w_h are respectively the length, the intermediate gap in length and the width of the heliostat, u_{hx}', u_{hy}' and u_{hz}' are respectively the positive unit vector of x-axis (length direction), y-axis (width direction) and z-axis (normal direction) of every individual heliostat coordinate system relative to the heliostat field coordinate system. It is possible to obtain multiple p_r due to the shadowing between the heliostats, of which the one corresponding to the minimum d_{ray} is the true solution.

The roughness of the heliostat surface should be considered. The surface roughness is simulated by the deviation of zenith angle ($d\theta_n'$) and azimuth angle ($d\varphi_n'$) of the actual normal direction ($\vec{n}$) from the ideal normal direction ($\vec{n}^*$), where $d\theta_n'$ obeys the Gaussian distribution with 0.1^o as the standard deviation and $d\varphi_n'$ obeys uniform distribution between $0 \sim 2\pi$. Therefore, the actual reflection direction ($\vec{r}$) deviating from the ideal reflection direction ($\vec{r}^*$) can be calculated by Eqs. (15)–(17).

$$\vec{r}^* = \vec{s} \Big/ \left[u_{hx}'; u_{hy}'; u_{hz}'\right] * \begin{bmatrix} 1 & 0 & 0 \\ 0 & 1 & 0 \\ 0 & 0 & -1 \end{bmatrix} * \left[u_{hx}'; u_{hy}'; u_{hz}'\right] \tag{15}$$

$$\vec{r}' = \left[sin(d\theta_n')cos(d\varphi_n'), sin(d\theta_n')sin(d\varphi_n'), cos(d\theta_n')\right] \tag{16}$$

$$\vec{r} = \vec{r}' * \left[u_{rx}'; u_{ry}'; u_{rz}'\right] \tag{17}$$

Here, u_{rx}', u_{ry}' and u_{rz}' are respectively the positive unit vector of x-axis, y-axis and z-axis of the coordinate system with $\vec{r}^*$ as the positive direction of z-axis, which can be obtained in a similar way of u_{sx}', u_{sy}' and u_{sz}'.

The determination of blocking between heliostats is the same as that of shadowing, except that p_e is replaced by p_a, and $\vec{s}$ is replaced the reverse direction of $\vec{r}$.

3.1.3. Aperture model

The target position (p_t), final direction ($\vec{r}$) and final energy (e) of each ray entering the aperture need to be recorded to couple the subsequent model of the receiver, and can be calculated by Eqs. (18)–(21).

$$p_t = p_r + \vec{r} * d_{ray} \tag{18}$$

$$(p_t - p_a) \cdot \vec{n}_{ap} = 0 \tag{19}$$

$$\eta_{att} = \begin{cases} 0.99321 - 0.0001176 d_{ray} + 1.97 \times 10^{-8} {d_{ray}}^2, d_{ray} \le 1\text{km} \\ e^{(-0.0001106 d_{ray})}, d_{ray} > 1\text{km} \end{cases} \tag{20}$$

$$e = DNI * A_{DNI} * \rho_h * \eta_{att} * d_{ray} / n_{ray} \tag{21}$$

Here, d_{ray} is the travel distance of ray from heliostat to aperture, η_{att} is the atmospheric attenuation factor, which is proposed by Leary et al. [42], DNI is the direct normal irradiance, A_{DNI} is the projected area of the sun-simulated plane in the direction of $\vec{s}$, ρ_h is the reflectivity of the heliostat, n_{ray} is the number of the simulated rays.

3.2. Receiving model

The schematic of the energy transfer model of the receiver are shown in Fig. 6. The domain of the receiver consists of three subdomains: the preheating channel with secondary reflective surface, the particles on the solar receiving slope and the connecting funnel. The main energy transfer forms include the incident power from heliostat, the radiation,

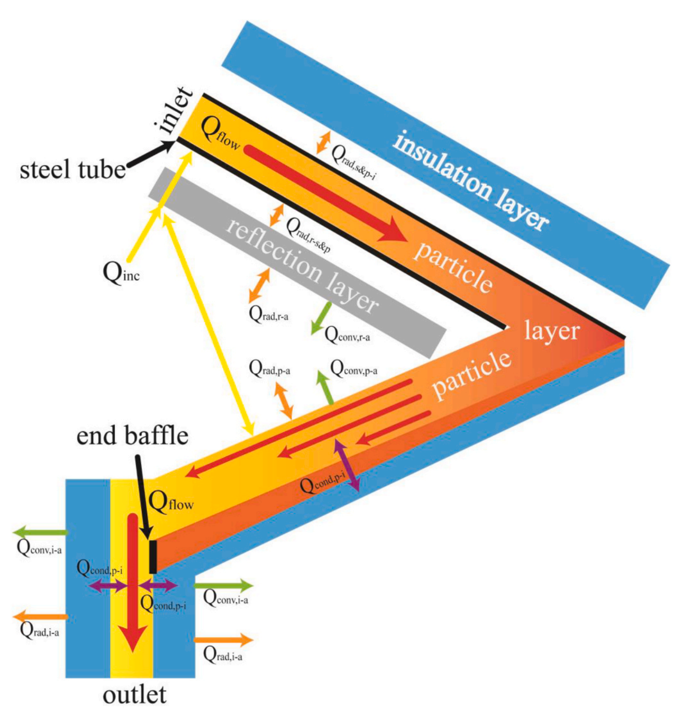

Fig. 6. The schematic diagram of the energy transfer model.

convection and conduction from the inner objects and particles of the receiver and the energy transfer by mass flow, which are distinguished by annotations and colors. The bidirectional arrows in the schematic represent the reciprocity of energy transfer, such as the secondary reflective surface that radiates outward while also receiving radiation from other planes. The meanings of the subscripts can be found in nomenclature. The steel tube and the particles flowing inside are regarded as isothermal radially due to the high thermal conductivity and small radius of the steel tube. The flowing particle layer on the slope is divided into 3 parts to simulate the temperature and flow rate distribution in the depth direction. The stagnant and flowing particle layer are separated by an end baffle. The particle flow is assumed to be continuous and dense. The sidewalls inside the receiving cavity are assumed to be isothermal due to sufficient thermal insulation measures.

Since Fig. 6 clearly illustrates the energy transfer relationship, the specific energy equations for each component will not be repeated here. Here, only the calculation method for particle temperature changes will be emphasized.

The energy equation of the particle flow in each control volume can be expressed by Eq. (22)

$$Q_p = Q_{flow} + Q_{rad,inc} + Q_{rad,inner} - Q_{rad,p} - Q_{conv,p} - Q_{cond,p} \tag{22}$$

Here, Q_p is the net power gained by particles, Q_{flow} is the heat transfer due to particle flow, $Q_{rad,inc}$ and $Q_{rad,inner}$ are the received radiation from incident rays and inner objects of the receiver, respectively, $Q_{rad,p}$, $Q_{conv,p}$ and $Q_{cond,p}$ are the radiation, convection and conduction loss of particles, respectively.

Q_{flow} is calculated by Eq. (23).

$$Q_{flow} = Q_{flow,in} - Q_{flow,out} = c_p \dot{m}_p (T_{in} - T_{out}) \tag{23}$$

Here, c_p is the average particle heat capacity between T_{in} and T_{out}, $\dot{m}_p$ is the particle mass flowrate, T_{in} and T_{out} are respectively the inlet particle temperature and outlet particle temperature for the control volume.

$Q_{rad,inc}$ and $Q_{rad,inner}$ are obtained by Monte Carlo method, which set the incident rays and the high temperature objects inside the receiver as the ray emitting source, respectively. During the ray tracing, the secondary reflective surface and sidewalls are regarded as the surfaces with roughness model as described as that of heliostats, and the surface of the particle flow is regarded as diffuse reflectance. The emitting directions of the rays obey the law of Lambert as expressed by Eq. (24) [43].

$$\frac{d\phi(\varphi, \theta)}{dA * \cos\theta * d\Omega} = I \tag{24}$$

Here, θ is the angle of zenith, φ is the angle of azimuth, A is the reflecting area, Ω is the spatial angle, I is the radiation intensity and ϕ is the radiation power. Therefore, according to the probability theory, θ and φ can be calculated by Eqs. (25) and (26) [44].

$$\theta = \frac{a\cos(1 - 2R)}{2} \tag{25}$$

$$\varphi = 2\pi * R \tag{26}$$

Here, R is a random number between 0 and 1.

$Q_{rad,p}$ is calculated by Eq. (27)

$$Q_{rad,p} = \sigma A_p \varepsilon_p T_p^4 \tag{27}$$

Here, σ is the Stefan-Boltzmann constant, A_p, ε_p and T_p are the heat transfer area, the emissivity and the temperature of particles, respectively.

$Q_{conv,p}$ is calculated by Eqs. (28)–(31) [45],

$$T_e = T_p - (T_p - T_a)/4 \tag{28}$$

$$Gr_e = g\beta l^3 (T_p - T_a)/\upsilon^2 \tag{29}$$

$$h = \frac{\lambda}{l} * \left(0.14 * \left((Gr_e\,Pr)^{\frac{1}{3}} - (Gr_c\,Pr)^{\frac{1}{3}}\right) + 0.56 * (Gr_e\,Pr * \cos(\theta))^{\frac{1}{4}}\right. \tag{30}$$

$$Q_{conv,p} = A_p h (T_p - T_a) \tag{31}$$

Here, T_p and T_a are respectively the temperature of the particles and ambient air, λ, Pr and υ are respectively the thermal conductivity, the Prandtl number and the kinematic viscosity coefficient of the ambient air which depend on the characteristic temperature T_e, β is calculated based on $T_a + (T_p - T_a)/4$, θ is the angle between the particle surface and the vertical direction, Gr_c is the critical Grashov number which depend on θ, h is the convection heat transfer coefficient, l is the characteristic length, g is gravity coefficient.

$Q_{cond,p}$ is calculated by Eq. (32).

$$Q_{cond,p} = A_p \lambda_p (T_p - T_i)/d \tag{32}$$

Here λ_p is the thermal conductivity of the particles, T_i is the temperature of the insulation materials (insulation cotton, stagnant particles, etc), d is the distance between the centres of the particle layer and insulation layer.

After obtaining Q_p, the temperature change of the particles within each time step can be calculated by Eq. (33).

$$\Delta T_p = Q_p \cdot \Delta\tau / (c_p A_p d_p \rho_p) \tag{33}$$

Here, $\Delta\tau$ is the time step, c_p, A_p, d_p and ρ_p are the heat capacity, the heat transfer area, the layer thickness, and the bulk density of particle flow respectively.

Therefore, the temperature of the particles ($T_{ave,out}$) can be obtained, and the receiver efficiency (η) are defined as Eq. (34)

$$\eta = (c_{ave,out} T_{ave,out} - c_{ave,in} T_{ave,in}) \dot{m}_{sum} / Q_{sum,inc} \tag{34}$$

Here, $\dot{m}_{sum}$ is the total mass flowrate of particle, $T_{ave,in}$, $T_{ave,out}$, $c_{ave,in}$ and $c_{ave,out}$ are the average temperatures and average heat capacities of the particles at the inlet and outlet of the particle receiver respectively, $Q_{sum,inc}$ is the total incident power.

In addition, the radiation, convection, thermal and optical loss rate (φ_{rad}, φ_{conv}, φ_{ther} and φ_{opt}) are defined as Eqs. (35)–(38),

$$\varphi_{rad} = Q_{rad}/Q_{sum,inc} \tag{35}$$

$$\varphi_{conv} = Q_{conv}/Q_{sum,inc} \tag{36}$$

$$\varphi_{ther} = \varphi_{rad} + \varphi_{conv} \tag{37}$$

$$\varphi_{opt} = Q_{opt}/Q_{sum,inc} \tag{38}$$

Here, Q_{rad} and Q_{conv} are respectively the radiation and convection loss from the receiver and internal particles, Q_{ther} is the loss due to the high temperature of the receiver and internal particles, which is the sum of Q_{rad} and Q_{conv}, Q_{opt} is the heat loss due to the incident ray escape.

η can also be expressed by Eq. (39).

$$\eta = 1 - \varphi_{opt} - \varphi_{ther} \tag{39}$$

When the steady state is not reached, the $\eta_{receiver}$ obtained from Eq. (34) and Eq. (39) are usually different. Here, the η calculated from Eq. (34) is termed the positive efficiency (η_p), while the η obtained from Eq. (39) is termed the negative efficiency (η_n).

4. Experiments and discussions

4.1. Experimental conditions

The experiments were conducted in Zhejiang University Qingshanhu Energy Research Center located in Hangzhou, which is a typical southern Chinese city with a rainy and moist climate. The heliostat field and tower used for experiments are shown in Fig. 7. Incident power ranging from 200 to 400 kW were provided by 75 heliostats. The receiver was fixed on the 7th floor of the tower, ~28 m in height. The aperture has a diameter of 1.5 m, and a water-cooled wall is installed around the aperture to protect the tower wall from being burned by the overflowing concentrated solar radiation.

The incident power distribution provided by the heliostat field can be obtained by a CCD-camera Lambertian method [46], and the concentrating model mentioned above was used in conjunction with actual measurements to derive incident power distribution for subsequent transient receiver performance analysis.

The total height of the receiver for testing was ~3.22m, in which the horizontal and vertical distances of the receiving cavity were both ~1.4m, with a depth of ~1.34m. The angle of the secondary reflective surface is ~30°, and the angle of the solar receiving slope is ~25°. The maximum total particle flow rate of the 5 valves is ~0.6 kg/s.

4.2. Flow pattern research

For better reliability and safety of the on-sun experiments, a transparent slope model composed of acrylic sheets was utilized to research the flow pattern of the particles in a cold-state condition as shown in Fig. 8(a). The flow pattern research mainly included the flow angle characteristics and the flow velocity distribution of the flowing particle layer.

4.2.1. Flow angle characteristics

The flow angle, or the angle of flow, specifically denoting the inclination angle of the particle layer surface under flowing conditions, was slightly different from the angle of repose as shown in Fig. 8(b and c), and the baffles installed at the end of slope would also make a difference. Therefore, despite the many studies on the angle of repose [47,48], there was still a need for this research.

The flow angle exhibited many characteristics similar to the repose angle, such as the decrease of flow angle caused by the concentration of particle size distribution. The following will not repeat these similar characteristics, but focus on the effects of the flowing and the baffle.

Fig. 7. A perspective view of the tower and heliostat field in Zhejiang University Qingshanhu Energy Research Center.

The influence of flowrates (FR) and baffle heights (HB) on the flow angle and the fluctuation of the particle layer is shown as Fig. 9, while the angle of repose is ~23.5°.

Based on the experimental observations and results, the following preliminary conclusions and analyses could be given below.

The angle of flow was always larger than the (stopping) angle of repose. Due to the fact that the particles were always in a flowing state, the particle pile was always affected by the impact of the flowing particles and could not be in repose.

The flowrate hardly affected the flow angle with a baffle.

The angle of flow with a baffle was larger than that without a baffle, and the baffle height hardly affected the angle of flow. The introduction of the baffles actually changed the roughness of the bottom surface where the particles flow, and the change of roughness affected the accumulation process [49], i.e. the particle flow pattern for current experiments. When there was no baffle, the bottom surface of the particle flow was an acrylic sheet. Due to the lower roughness of the acrylic sheet than the critical roughness, almost the whole flowing particle layer would undergo the leaving and replenishment of particles. When there was a baffle, the bottom surface of the particle flow became the stagnant particle layer with a roughness greater than the critical roughness, and the particles closer to the surface underwent more leaving and replenishment of particles while the particles closer to the bottom almost stayed still. Obviously, the particle flow state with a baffle was closer to the state of repose than that without a baffle, resulting a larger angle. In addition, regardless of how high the baffle was, the bottom surface of the particle flow would always be composed of stagnant particles, and thereby the angle of flow was hardly affected by the change of baffle height.

There was a tidal fluctuation characteristic of the particle flow. Increasing the baffle height and reducing the flowrate would enhance the amplitude of fluctuation. The fluctuation originated from the leaving and replenishment of particles. The particles along the flow direction did not flow down simultaneously. In fact, the particles located lower along the flow direction flowed away earlier than those located higher, in other word, the leaving was generally sooner than the replenishment, resulting in the gradual decrease of particles, similar to a falling tide. Until the lower particles were not enough to support the entire flowing particle layer, the whole particle layer collapsed rapidly, which was similar to a rising tide. Then, the "falling tide" would be repeated. In addition, the fluctuation exhibited significant randomness, particularly during the early stages.

4.2.2. Flow velocity distribution

An image processing method based on tracer particles were used to research the particle flow velocity distribution at different depths of the flowing particle layer. The research methodology employed was detailed as follows: tracer particles, which had been dyed for enhanced visibility, were introduced into a transparent slope model. Real-time imaging techniques were utilized to capture the flow behavior of these tracer particles. Subsequent to the imaging process, a frame-by-frame analysis was conducted to derive the velocity distribution of the particles across different depths within the model.

The preliminary experimental results and the fitting curve are shown as Fig. 10, and the fitting function is described by a double Gaussian function as Eq. (40).

$$y = \eta_{flowrate} * \left(4e^{-\left(\frac{x-9.8}{4.6}\right)^2} - e^{-\left(\frac{x-7.2}{2}\right)^2}\right) \tag{40}$$

Here, x is the relative position, where 0 and 9 correspond to the bottom and top surfaces of the flowing particle layer, respectively, $\eta_{flowrate}$ is the correction factor based on flowrate, where a higher flowrate results in a larger the $\eta_{flowrate}$, y is the flow velocity.

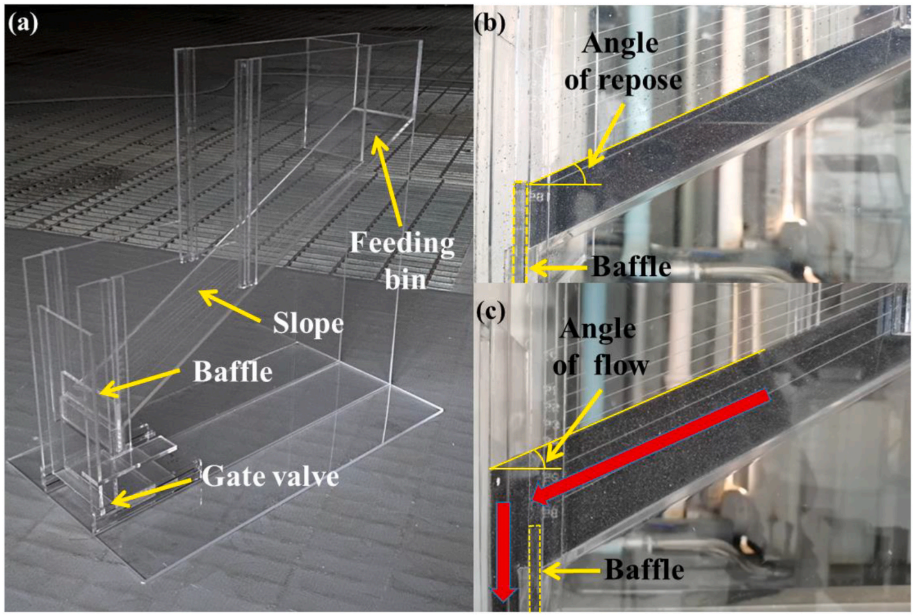

Fig. 8. Transparent slope model (a), the angle of repose (b) and the angle of flow (c).

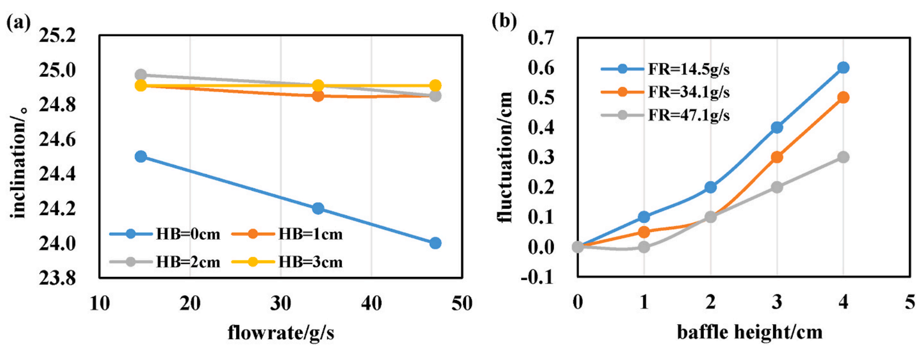

Fig. 9. The influence of flowrates and baffle heights on the flow angle (a) and the fluctuation (b) of the particle layer.

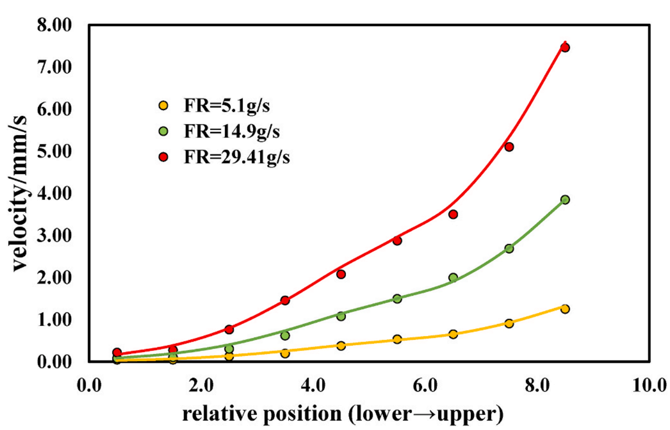

Fig. 10. Flow velocity distribution of the flowing particle layer with different flowrate.

Based on the experimental observations and results, the following preliminary conclusions and analyses could be given below.

Due to the drag effect of stagnant particles, the very bottom particles had almost no flow velocity, and as the position got closer to the surface of the particle layer, the flow velocity gradually increased. Based on the flow velocity distribution, the flowing particle layer could be divided into surface, middle, and bottom layers, with corresponding flowrates of approximately 67.6 %, 26.9 %, and 5.5 % of the total flowrate, respectively. Due to the poor thermal conductivity of particles, the heat obtained by the particles of the bottom layer was much lower than that of the surface layer. However, the heating time for the bottom particles was extended with a lower flowrate, which reduced the temperature difference between the surface and bottom layer and was beneficial for the average temperature rise of the whole flowing particle layer. And the high flow velocity of surface particles also helped reduce the risk of local overheating.

The flowrate hardly changed the relative distribution of the flow velocity, but changed the absolute value of the flow velocity, where a higher flowrate resulted in a higher flow velocity.

It should be noted that the aforementioned flow pattern analysis is primarily based on qualitative explanations of experimental phenomena. More specific quantitative analyses and simulations remain to be carried out in the future.

4.2.3. Research significance

- The measurement of flow angle can assist in the design of parameters such as the slope inclination and the baffle height, to avoid the stoppage which is usually caused by a too high baffle. In practical designs, the inclination of the slope is preferably set to be 5° or even more above the flow angle, and then the thickness of the flowing particle layer can be adjusted by the height of baffle. Because once the flow angle decreases due to the dust pollution or other reasons, the replacement of a small baffle is much easier than the adjustment of the whole slope.

- The study of the flow angle characteristic is beneficial for the experimental operation of the receiver. For example, the baffle height and flowrate hardly affect the flow angle. As a result, the thickness of the flow layer can be precisely adjusted by adjusting the baffle height, and the flowrate can be adjusted freely with very little risk of particles failing to cross the baffle. It is noteworthy that the very little risk mentioned comes from the fluctuation, which can be enhanced by the decrease in flowrate. Considering the significant randomness of the fluctuation, it is necessary to ensure that particles can cross the baffle during sufficient number of fluctuation cycles, especially during the troughs.
- The flow velocity distribution can serve as an input parameter for simulations. Specifically, grids at different depths can correspond to different particle flowrates, thereby enhancing the accuracy of simulation results.

4.3. On-sun experiments

4.3.1. Experimental approach

Before the on-sun experiments, a cold-state commissioning would be conducted to identify potential faults, and some experimental conditions would be set in advance, such as the thickness of the particle layer by adjusting the baffle heights and the particle flowrate by adjusting the gate valves. Once the on-sun experiments started, the heliostat would firstly perform the sun-tracking process. As the amount of heliostats completing the sun-tracking process increased, the incident solar radiation and the particle temperature would increase. During this period, key data such as temperature and flowrate would be recorded, and control devices such as gate valves would be operated in real time. Currently, particles leaving the receiver would pass through a high-temperature storage bin, a heat exchanger, a low-temperature storage bin, and a particle lifting device, and then got back to the receiver. It should be noted that the above-mentioned equipment such as the exchanger only served the function of transporting.

4.3.2. Secondary reflective surface tests

Due to the direct exposure to the concentrated solar radiation, the geometric design and material selection for the secondary reflective surface was very strict.

The aluminum silicate fiberboard with a temperature resistance of 1260 °C and a reflectivity of ~70 % was firstly tested. On-sun tests showed that when using one large piece of aluminum silicate fiberboard as the secondary reflective surface, the pressure caused by the particles weight, as well as the significant thermal deformation caused by the large size would cause local cracks. When using multiple aluminum silicate fiberboards to piece together into one single secondary reflective surface, the gaps between the fiberboards were difficult to ensure the particle sealing after several cycles of thermal expansion and contraction as shown in Fig. 11(a). In addition, the aluminum silicate fiberboard has high thermal insulation, which is not suitable for preheating the particles. Therefore, this scheme was abandoned. Then, an array of ceramic tubes with a temperature resistance of 1600 °C and a reflectivity of ~80 % was tested, as shown in Fig. 11(b). Although ceramic tubes with 99 % Al2O3 had extremely high temperature resistance, the situation with drastic changes in temperature, such as a sudden cloud cover, could easily cause local cracks. Therefore, this scheme was also abandoned. The final and currently proven effective solution was to use a combination of high-silica fabric and 310s stainless steel tube array as shown in Fig. 11(c and d). The high-silica fabric has a temperature resistance of 1250 °C, a reflectivity of ~83 %, and a transmittance of ~7 %, which

Fig. 11. Secondary reflective surface using aluminum silicate fiberboards (a), ceramic tube array (b) and the combination of high-silica fabric and 310s stainless steel tube array (c–d).

could simultaneously reflect incident rays and preheat the particles flowing inside the stainless steel tubes with the transmitted rays. Due to the flexibility of high-silica fabric and the robustness of stainless steel, the combination of both exhibited strong high-temperature reliability. Fig. 11(d) shows the receiver state after a manual removal of high-silica fabric. The deformation of the stainless steel tube in the middle was caused by the accidental damage to the corresponding high-silica fabric during installation, while the stainless steel tubes in other locations were still in good condition, which indirectly proved the protective effect of high-silica fabric on the stainless steel tubes. Coating the stainless steel pipes with Al2O3 seems to have better effect than the high-silica fabric, but there are still some issues to be verified, such as the peeling risk of coating.

4.3.3. Typical cases and discussions

After determining the structural design of the secondary reflective surface, the on-sun experiments could be conducted. The scene of an on-sun experiment and some heated particles flowing out of a gate valve are illustrated in Fig. 12.

Several on-sun experiments have been conducted, and the one conducted on July 12, 2023 achieved the highest recorded outlet temperature due to good DNI condition. Specifically, the maximum outlet temperature of ~860°C was achieved by the 3rd outlet with DNI of ~851W/m^2, flowrate of ~83.5 g/s and initial particle layer thickness of ~3 cm. Fig. 13 shows the real-time changes in temperature and DNI for the 3rd part of the receiver in this experiment.

Based on the relatively stable state at 14:08, the temperature of the particles entering the receiver was ~350°C. After being preheated and directly heated, the particles finally left the 3rd outlet of the receiver at ~860°C. The single-pass temperature rise was up to ~510°C, i.e. ~340 °C/m in vertical direction. The temperature of the measurement point on the secondary reflective surface was ~830 °C, which was well below the safe operating temperature of high-silica fabric. In addition, for all five parts of the receiver, the average outlet temperature on energy weighted was ~782°C, in which the outlet temperatures of the edge parts were lower than the average value due to the relatively lower view factor for the incident rays.

The overall temperature rise trend was rapid at first and then slow. The rapid rise in temperature at first was due to the gradual completion of the heliostat tracking process, resulting in a rapid rise in incident solar radiation. The slow temperature rise in the middle and later stages could be attributed to several factors, including 1) the gradual increase in temperature of the receiver's internal structure, 2) the gradual increase in temperature of the inlet particles after repeated heating cycles and 3) the slight increase in the heliostat efficiency and thus the incident solar radiation.

Several significant decrease in temperature were observed after the decrease in DNI. The influence of DNI on the outlet temperature has a time lag due to the time required for particles to flow from the receiving cavity to the outlet.

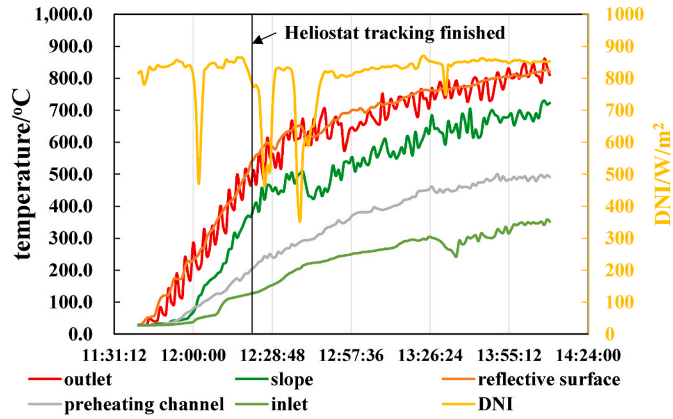

Fig. 13. Real-time changes in temperature and DNI for the 3rd part of the receiver.

For the measurement point at inlet, a sudden temperature rise occurred at ~12:08, which was due to first returning of the heated particles through external circulation. And a sudden temperature drop occurred at 13:26, which was due to the direct exposure of the thermocouple to the air. After increasing the particles feeding in, the thermocouple was reburied and thereby the temperature rose. For the measurement points at slope and outlet, significant fluctuations were observed. However, the fluctuations were more attributable to the measurement method than to the temperature variations of the particles. Specifically, the thermocouple used to measure the particle temperature on the slope was slightly buried by the flowing particles, to avoid being directly exposed to and heated by the solar radiation. However, as mentioned in the previous study on flow patterns, the thickness of the flowing particle layer has tidal fluctuation characteristic, which means the particles covering the thermocouple would vary in thickness, resulting in the fluctuations in measured value. The thermocouple used to measure the outlet temperature was placed at the bottom of the weighing bin. When the weighing bin was about to be filled, the particles inside would be unload, exposing the thermocouple to the air and causing a sharp drop in measurement. When the bottom of the weighing bin was refilled by high-temperature particles, the thermocouple was reburied and the temperature rose sharply.

To better depict the rise trend of particle temperature at outlet, measurement values with sudden drops were excluded, and the coupled concentrating-receiving model proposed in this paper was used to simulate and analyze the temperature rise curve. The specific conditions used in simulation is shown in Table 2. The comparison between simulation and experimental results for the 3rd and 5th outlet is shown in Fig. 14, which shows relatively good fitting accuracy.

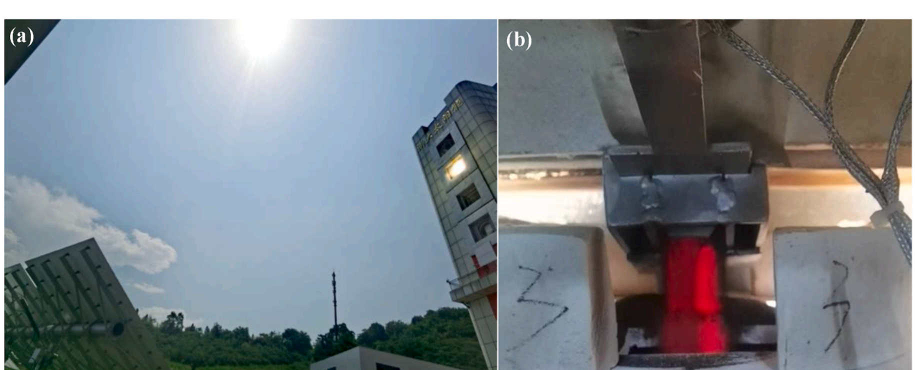

Fig. 12. On-sun experiment scene (a) and some heated particles flowing out of a valve (b).

Table 2
Some of the conditions for simulation.

parameters	value
reflectivity of the secondary reflective surface	82.5 %
transmissivity of the secondary reflective surface	7 %
thickness of the flowing particle layer	~3 cm
grid size along the transverse direction	~1.72 cm
grid size along the flow direction	~1.8 cm
grid size along the depth direction	~1 cm
ray number generated from each single grid	10000
ambient temperature	28.5°C
fitting formula for c_p	$c_p = 456.3 * T^{0.1569}$

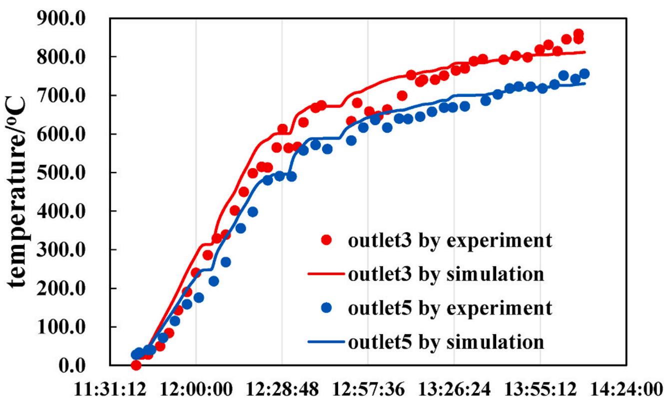

Fig. 14. The comparison between simulation and experimental results.

For the early and middle stages of the temperature rise curve, the simulation results were close to but always slightly higher than the experimental results, and exhibited a slightly faster temperature rise rate, which might be due to the underestimation of the heat loss and heat capacity of the receiver. In the final stage, the simulation curve tended to stabilize, but the experimental curve was still gradually increasing. To find out the reason for the temperature rise in the final stage, the concentrated solar radiation was quickly removed to facilitate the direct observation of the flowing particles at high temperature. The thickness of the particle layer was found to be significantly lower than the initial value of ~3 cm, which explains the difference between the simulation and experimental values in the final stage. In fact, the reduction of particle layer thickness was not accidental, but an inevitable phenomenon caused by the reduced fluidity of particles at high temperature. Similar situations were also observed in other on-sun experiments, and with the increase of temperature, the reduction in thickness became more significant. The specific effect and mechanism of high temperature on particle flow pattern remained to be further studied. For the current experiments, sufficient particle layer thickness allowance should be reserved to prevent the stoppage of particle flow.

Based on the experimental results, the simulation process was optimized and calibrated, and then the time-dependent parameters such as the loss rates and efficiencies for the 3rd part of the receiver were obtained through experimental measurements and simulation calculations as shown in Fig. 15.

The change in DNI directly led to the change in incident power, which served as the denominator in the calculation of loss rates and efficiencies. Therefore, when DNI decreased sharply, due to the time lag of the change in outlet temperature, the positive efficiency would experience a sharp increase such as the situation at 12:00. Obviously, the loss rates and efficiencies under a stable state, especially under a stable DNI were more worth referring. During the final and relatively stable stage, the total incident power and the maximum incident flux reached ~350 kW and ~400kW/m2 on aperture respectively. The positive and negative efficiency for the 3rd part of the receiver reached

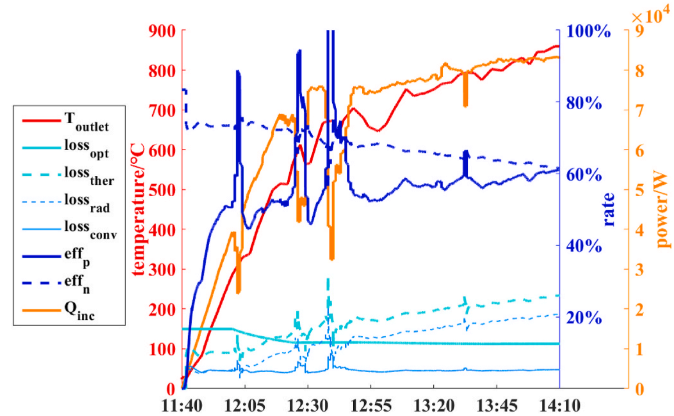

Fig. 15. The time-dependent changes of outlet temperature, optical loss rate, thermal loss rate, radiation loss rate, convection loss rate, positive efficiency, negative efficiency and incident power for the 3rd part of the receiver.

~60.9 % and ~61.5 % respectively, with radiation loss rate of ~20.7 %, convection loss rate of ~5.3 % and optical loss rate of ~12.5 %. And for the overall receiver, the positive and negative efficiency were ~56.8 % and ~59.0 % respectively, with radiation loss rate of ~21.6 %, convection loss rate of ~6.9 % and optical loss rate of ~12.5 %.

The fundamental difference between positive and negative efficiency lied in whether or not to consider the solar absorption by the receiver's internal structure as a loss. Positive efficiency viewed it as a loss, while negative efficiency did not. As the solar receiving process reached a stable state, the internal structure no longer rose in temperature, and the positive and negative efficiency tended to be equal. Generally speaking, positive efficiency was more intuitive for evaluating the receiver performance, while negative efficiency is more convenient for analyzing the impact of various heat losses.

In the various loss rates, the optical loss rate decreased firstly and stabilized later. In the initial stage, based on program settings, heliostats located closer to the tower completed their sun-tracking process earlier, and thereby the directions of the incident rays were more vertical at first. The geometric structure of the receiver made these more vertical incident rays more susceptible to being directly reflected out, resulting a higher optical loss rate. Later on, as all the heliostats finished the sun-tracking process, the optical loss rate gradually decreased and finally stabilized. The ultimate optical loss rate was primarily determined by the geometric structure of the receiver and the optical properties of the structure's materials, but was not directly affected by temperature. The thermal loss rate, including the radiation and convection loss rate (the conduction loss rate was ignored in this simulation), was directly affected by temperature. The higher the temperature was, the greater the thermal loss was, and the radiation loss was directly proportional to the fourth power of temperature, indicating a more pronounced influence from temperature.

Some typical on-sun experimental results are shown in Table 3, in which the parameters were basically selected under relatively stable states.

The optical loss rate was found to be inversely related to the proximity of the date to the summer solstice, with lower rates observed as the date approached the summer solstice, and conversely, higher rates as the date neared the winter solstice. However, this variation was relatively minor when compared to the thermal loss rate. For our current testing setup, the thermal loss rate exerted a more significant influence on the receiving efficiency, with radiation loss contributing more substantially than convection loss. For case 3 and case 5, the similarity in date, time, and DNI led to a close incident power. Nonetheless, the flow rate of case 5 was notably higher than that of case 3, which resulted in differing temperatures and efficiencies. Specifically, with a constant incident power, the elevated flow rate in case 5 diminished the amount of

Table 3
Summary of on-sun experimental results.

Case	1	2	3	4	5
Date	10.22	7.12	6.10	5.25	5.15
Time	14:18	14:10	14:11	15:00	14:47
DNI (W/m2)	629.1	851.6	641.9	686.4	664.2
incident power(kW)*	175	350	267	275	263
Mass flow rate (g/s)	262.7	420.7	309.8	340.0	424.9
Average outlet temperature (°C)	535	782	753	707	651
maximum outlet temperature (°C)	595	860	814	749	689
Temperature rise (°C)	302	430	410	382	346
optical loss rate*	12.4 %	12.5 %	13.0 %	12.7 %	12.7 %
thermal loss rate*	30.0 %	28.5 %	30.6 %	29.3 %	24.8 %
radiation loss rate*	19.1 %	21.6 %	21.9 %	20.9 %	16.6 %
convection loss rate*	10.9 %	6.9 %	8.7 %	8.4 %	8.2 %
Negative efficiency*	57.6 %	59.0 %	56.5 %	58.1 %	62.5 %
Positive efficiency	51.4 %	56.8 %	58.6 %	59.4 %	66.1 %

Note: *: simulated value.

incident radiation absorbed by each particle, leading to a reduced temperature rise per particle and an overall lower temperature for case 5. The lower temperature corresponded to a decreased thermal loss rate, where the reduction in radiation loss was more pronounced than that of convection loss. For case 1 and case 2, case 1, being closer to the winter solstice, experienced a decline in both DNI and heliostat efficiency, resulting in an incident power that was only about half that of case 2. Although the overall temperature in case 1 was lower, resulting in lower radiation and convection loss in absolute value than those in case 2, the much more significant decrease in incident power, as the denominator in loss rate calculations, resulted in a higher radiation and convection loss rate in case1. It is important to note that due to the lower ambient temperature, the proportion of convection loss in case 1 was higher than that in other cases.

In summary, increasing the incident power could effectively improve receiving efficiency. While increasing the flow rate may lead to a reduction in the temperature rise of the particles, it could also indirectly contribute to a decrease in the thermal loss rate, thereby improving receiving efficiency.

4.3.4. Simulated prediction

Due to the limitation of the heliostat field size on the test site, cases with higher incident power, which was provided by more heliostats such as a commercial tower concentrating system, was simulated for the prediction of the receiver performance. Taking case 2 as the benchmark, the cases with 2, 3 and 5 times the experimental incident power, and 2.2, 3.5 and 6 times the experimental mass flow rate were analyzed by simulation.

As shown in Fig. 16, even though the temperature of the receiver increased, thermal loss rate (convection and radiation) gradually decreased from 28.48 % to 13.22 % due to the increase in incident power. The optical loss rate remained unchanged for that the geometric structure and the optical properties of the relevant materials were set unchanged in the simulation. The combined effect of thermal and optical loss rate resulted in an increase in the total positive efficiency from 56.8 % to 74.5 %. In a sense, with the increase of incident power, the thermal loss rate could be infinitely decreased, while the optical loss rate restricted the efficiency limit of the receiver. Optimizing the geometric structure and selecting materials with better optical properties, such as the particles with higher absorptivity and the secondary reflective surfaces with higher reflectivity, would have the potential to further improve the receiver efficiency.

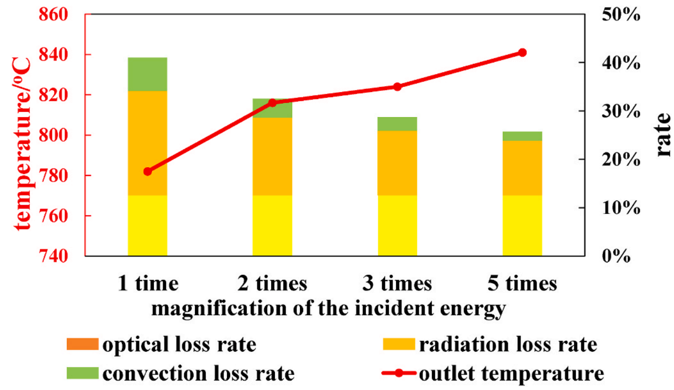

Fig. 16. Comparisons of loss rates with different incident power.

The temperature distribution with different magnification of incident power predicted by simulation is shown in Fig. 17, wherein, the surfaces, from top to bottom, are the preheating flow channel, the secondary reflective surface, and the surface, middle and bottom layer of the flowing particle. Obviously, with the magnification of incident power, the temperature of the receiver would increase. Specifically, the particle temperature could be adjusted effectively by the control of particle mass flow rate. However, the secondary reflective surface would experience a significant increase in temperature due to the lack of an effective cooling method. The maximum temperature on the secondary reflective surface would increase from 864 °C to 1215 °C, and eventually to 1416 °C with the max incident flux of ~500 kW/m^2 to ~1500 kW/m^2 and eventually to ~2500 kW/m^2, which exceeded the safe operating temperature of high-silica cloth. According to the above calculation, 1600 kW/m2 was approximately the limitation of the incident power for the current secondary reflective surface. The limitation could be further raised by adopting additional cooling methods such as a wind cooling, as well as coating the outer walls with high-temperature and high-reflectivity materials. In short, increasing the incident power could effectively improve the receiver efficiency, but it was very important to pay attention to the safety of the internal components, especially the secondary reflective surface.

In addition, the temperature distribution in the depth direction with different magnification of incident power was also predicted by simulation as shown in Fig. 17, which was difficult and actually failed to be obtained by experiments due to the tidal fluctuation characteristic of particle flow. The average temperature difference between the surface and bottom layer at the end of the slope were ~384 °C, and the difference would be increased to 512 °C and 534 °C as the incident power increased to 3 and 5 times the original value. No matter how much the incident power was, the large temperature difference due to the low thermal conductivity of particles limited the average outlet temperature and increased the overheating risk of the particles at surface. How to minimize the thickness of particle layer while ensuring stable flow is of great significance for the efficient and safe operation of receiver.

5. Conclusions and future work

In this paper, a modified sliding-bed particle solar receiver with an internal secondary reflection structure was proposed to realize the coupling with upward concentrating system, which was a challenge for the previous designs. Some cold-state flow pattern research and on-sun experiments were conducted to evaluate performance of the receiver. A concentrating-receiving coupled model was proposed to obtain the hard-to-measure data like heat loss composition and to predict the receiver performance under higher incident power. The specific conclusions are listed below:

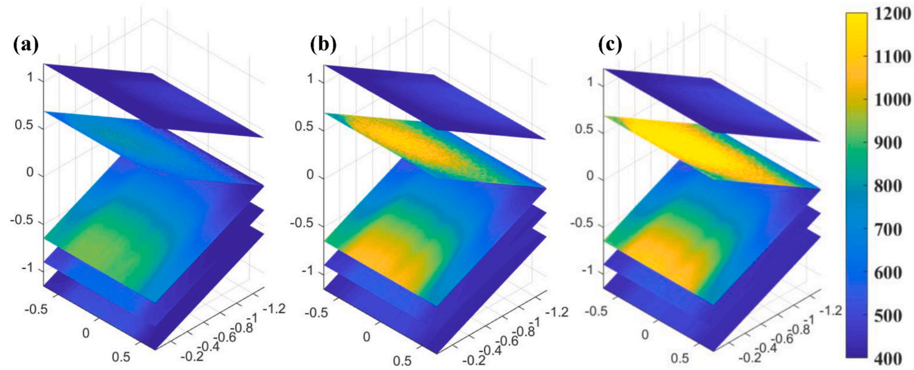

Fig. 17. Comparisons of temperature distribution with 1 time, 3 times and 5 times the experimental incident power of case 2.

1. The cold-state research on flow pattern showed that the flow angle was significantly affected by the installation of end baffle but hardly affected by flowrate, and particle flow velocity would increase as the position got closer to the layer surface.
2. The combination of high-silica fabric and stainless steel tube array for the secondary reflective surface exhibited strong high-temperature reliability under concentrated solar radiation.
3. In a typical on-sun experiment, the maximum outlet temperature reached ~860°C, the single-pass temperature rise reached ~510°C, and meanwhile the positive efficiency reached ~60.9 % with DNI of ~851W/m^2 and flowrate of ~83.5 g/s for the 3rd part of the receiver.
4. For several on-sun experiments under various DNI and time, the average outlet temperature ranging from ~535 °C to 782 °C, and positive efficiency ranging from ~51 % to 66 % were observed. Results showed that higher incident power, higher mass flow rate, and lower temperature could improve the receiver efficiency.
5. The model predicted that that the thermal loss rate could be reduced from 28.48 % to 13.22 % with 5 times magnification of the incident power, but the local overheating risk of the secondary reflective surface required attention.
6. The model indicated a large temperature difference due to the low thermal conductivity of particles, which limited the average outlet temperature and increased the overheating risk.

For such a complex and large-scale receiver research, especially for the on-sun experiments, there were many issues to be solved and improved, both in design and implementation. The work worth doing in the future is as follows:

1. Due to the decrease in particle fluidity observed in on-sun experiments, it is necessary to study the flow pattern of particles under high temperature to ensure the safety and stability of the receiver in practical operation.
2. The thermal insulation should be further improved, especially at the inlet and outlet of the receiver, to reduce the temperature fluctuations in the experimental results, and further enhance the temperature and efficiency of the receiver.
3. The challenges in large-scale design, such as the design for a 50MWe tower-type solar thermal power generation system, should be addressed, especially for the structural renovation of the secondary reflective surface to allow higher incident power, such as adding extra cooling methods and coating outer walls with high-temperature and high-reflectivity materials.

CRediT authorship contribution statement

Xiangyu Xie: Writing – review & editing, Writing – original draft, Visualization, Resources, Methodology, Data curation, Conceptualization. **Peiwang Zhu:** Writing – review & editing, Conceptualization. **Mingjiang Ni:** Supervision. **Fengyuan Chai:** Supervision. **Jiasong Li:** Supervision. **Gang Xiao:** Supervision, Conceptualization.

Declaration of competing interest

The authors declare that they have no known competing financial interests or personal relationships that could have appeared to influence the work reported in this paper.

Acknowledgements

The authors gratefully acknowledge the support from the National Natural Science Foundation of China (52325605), Key R&D Program of Zhejiang (NO. 2022C01043) and the Fundamental Research Funds for the Central Universities (2022ZFJH04).

Appendix A. Supplementary data

Supplementary data to this article can be found online at https://doi.org/10.1016/j.renene.2024.121275.

References

[1] C.K. Ho, B.D. Iverson, Review of high-temperature central receiver designs for concentrating solar power, Renew. Sustain. Energy Rev. 29 (2014) 835–846.
[2] F. Nie, F. Bai, Z. Wang, X. Li, R. Yang, Solid Particle Solar Receivers in the Next-generation Concentrated Solar Power Plant, EcoMat, Beijing, China, 2022, p. 4.
[3] K. Jiang, X. Du, Y. Kong, C. Xu, X. Ju, A comprehensive review on solid particle receivers of concentrated solar power, Renew. Sustain. Energy Rev. 116 (2019) 109463.
[4] C.K. Ho, A review of high-temperature particle receivers for concentrating solar power, Appl. Therm. Eng. 109 (2016) 958–969.
[5] J.M. Hruby, B.R. Steele, Solid particle central receiver for solar energy, Chem. Eng. Prog. 82 (1986) 44–47.
[6] A. Le Gal, B. Grange, M. Casanova, A. Perez, W. Baltus, M. Tessonneaud, G. Flamant, Experimental results for a MW-scale fluidized particle-in-tube solar receiver in its first test campaign, Sol. Energy 262 (2023) 111907.
[7] I. Perez Lopez, H. Benoit, D. Gauthier, J.L. Sans, E. Guillot, G. Mazza, G. Flamant, On-sun operation of a 150 kWth pilot solar receiver using dense particle suspension as heat transfer fluid, Sol. Energy 137 (2016) 463–476.
[8] G. Flamant, D. Gauthier, H. Benoit, J.-L. Sans, R. Garcia, B. Boissière, et al., Dense suspension of solid particles as a new heat transfer fluid for concentrated solar thermal plants: on-sun proof of concept, Chem. Eng. Sci. 102 (2013) 567–576.
[9] E. Johnson, D. Baker, I. Tari, Proposal of a Novel Gravity-Fed, Particle-Filled Solar Receiver, vol. 1850, 2017 030028.
[10] D.C. Miller, C.J. Pfutzner, G.S. Jackson, Heat transfer in counterflow fluidized bed of oxide particles for thermal energy storage, Int. J. Heat Mass Tran. 126 (2018) 730–745.
[11] K. Jiang, F. Wang, Y. Kong, C. Xu, X. Du, Characteristics of axial and radial development of solids holdup in a countercurrent fluidized bed particle solar receiver, J. Therm. Sci. 30 (2021) 2223–2240.
[12] J. Martinek, T. Wendelin, Z. Ma, Predictive performance modeling framework for a novel enclosed particle receiver configuration and application for thermochemical energy storage, Sol. Energy 166 (2018) 409–421.
[13] J. Martinek, Z. Ma, Granular flow and heat-transfer study in a near-blackbody enclosed particle receiver, J. Sol. Energy Eng. 137 (2015) 051008, 9.

[14] N.P. Siegel, C.K. Ho, S.S. Khalsa, G.J. Kolb, Development and evaluation of a prototype solid particle receiver: on-sun testing and model validation, J. Sol. Energy Eng. 132 (2010) 021008, 8.

[15] C.K. Ho, J.M. Christian, J.E. Yellowhair, K. Armijo, On-sun performance evaluation of alternative high-temperature falling particle receiver designs, J. Sol. Energy Eng. 141 (2019).

[16] C.K. Ho, J. Christian, J. Yellowhair, S. Jeter, M. Golob, C. Nguyen, et al., Highlights of the high-temperature falling particle receiver project: 2012 - 2016, AIP Conf. Proc. 1850 (2017).

[17] C.K. Ho, J.M. Christian, J. Yellowhair, N. Siegel, S. Jeter, M. Golob, et al., On-sun testing of an advanced falling particle receiver system, AIP Conf. Proc. 1734 (2016) 030022.

[18] C.K. Ho, J.M. Christian, J. Yellowhair, K. Armijo, Performance Evaluation of a High-Temperature Falling Particle Receiver, American Society of Mechanical Engineers, 2016.

[19] J.-S. Kim, A. Kumar, C.K. Ho, Multi-stage Falling Particle Receivers, 2023.

[20] J.-S. Kim, W. Gardner, D. Potter, Y.C.S. Too, Design of a multi-stage falling particle receiver with truncated-cone geometry, AIP Conf. Proc. 2303 (2020).

[21] J.-S. Kim, A. Kumar, W. Gardner, W. Lipiński, Numerical and experimental investigation of a novel multi-stage falling particle receiver, AIP Conf. Proc. 2126 (2019).

[22] L. Yue, N. Schroeder, C.K. Ho, Particle Flow Testing of a Multistage Falling Particle Receiver Concept: Staggered Angle Iron Receiver (STAIR), American Society of Mechanical Engineers, 2020.

[23] R. Shaeffer, B. Mills, L. Yue, C.K. Ho, Evaluation of performance factors for a multistage falling particle receiver. ASME 2020 14th International Conference on Energy Sustainability, 2020.

[24] B.H. Mills, C.K. Ho, N.R. Schroeder, R. Shaeffer, H.F. Laubscher, K.J. Albrecht, Design evaluation of a next-generation high-temperature particle receiver for concentrating solar thermal applications, Energies 15 (2022) 1657.

[25] C.K. Ho, N.R. Schroeder, H.F. Laubscher, L. Yue, B. Mills, R. Shaeffer, et al., Receiver design and On-Sun testing for G3P3-USA, AIP Conf. Proc. 2445 (2022).

[26] M. Lubkoll, M. Ebert, L. Amsbeck, A. Hirt, C. Frantz, J. Rheinländer, R. Buck, Development progress of the CentRec® particle receiver technology, AIP Conf. Proc. 2445 (2022).

[27] L. Amsbeck, R. Buck, M. Ebert, B. Gobereit, J. Hertel, A. Jensch, et al., First tests of a centrifugal particle receiver with a 1m2 aperture, AIP Conf. Proc. 2033 (2018) 040004.

[28] W. Wu, L. Amsbeck, R. Buck, R. Uhlig, R. Ritz-Paal, Proof of concept test of a centrifugal particle receiver, Energy Proc. 49 (2014) 560–568.

[29] Y. Yu, F. Bai, Z. Wang, Numerical and experimental investigation on thermal performances of quartz tube gravity-driven solid particle solar receiver based on linear-focused solar furnace, Renew. Energy 203 (2022) 881–897.

[30] Y. Yu, F. Hu, F. Bai, Z. Wang, On-sun testing of a 1 MWth quartz tube bundle solid particle solar receiver, Renew. Energy 193 (2022) 383–397.

[31] T. Wang, F. Bai, S. Chu, X. Zhang, Z. Wang, Experiment study of a quartz tube falling particle receiver, Front. Energy 11 (2017) 472–479.

[32] G. Xiao, K. Guo, M. Ni, Z. Luo, K. Cen, Optical and thermal performance of a high-temperature spiral solar particle receiver, Sol. Energy 109 (2014) 200–213.

[33] G. Xiao, K. Guo, Z. Luo, M. Ni, Y. Zhang, C. Wang, Simulation and experimental study on a spiral solid particle solar receiver, Appl. Energy 113 (2014) 178–188.

[34] S. Padula, M. Troiano, C. Tregambi, R. Solimene, P. Salatino, Directly irradiated fluidized bed autothermal reactor (DIFBAR): hydrodynamics, thermal behaviour and preliminary reactive tests, Fuel 346 (2023) 128222.

[35] C. Tregambi, S. Padula, M. Galbusieri, G. Coppola, F. Montagnaro, P. Salatino, et al., Directly irradiated fluidized bed reactor for thermochemical energy storage and solar fuels production, Powder Technol. 366 (2020) 460–469.

[36] X. Xie, H. Xu, D. Gan, M. Ni, J. Yan, K. Cen, G. Xiao, A sliding-bed particle solar receiver with controlling particle flow velocity for high-temperature thermal power generation, Renew. Energy 183 (2022) 41–50.

[37] X. Xie, G. Xiao, M. Ni, J. Yan, H. Dong, K. Cen, Optical and thermal performance of a novel solar particle receiver, AIP Conf. Proc. 2126 (2019) 030065.

[38] E. Koepf, S.G. Advani, A. Steinfeld, A.K. Prasad, A novel beam-down, gravity-fed, solar thermochemical receiver/reactor for direct solid particle decomposition: design, modeling, and experimentation, Int. J. Hydrogen Energy 37 (2012) 16871–16887.

[39] I. Reda, A. Andreas, Solar position algorithm for solar radiation applications, Sol. Energy 81 (2007) 838.

[40] T. Wendelin. Soltrace: A New Optical Modeling Tool for Concentrating Solar Optics. pp. 253-260.

[41] F. Biggs, C.N. Vittltoe, Helios Model for the Optical Behavior of Reflecting Solar Concentrators, 1979.

[42] P.L.H. Leary, J. D. User's Guide for MIRVAL: a Computer Code for Comparing Designs of Heliostat-Receiver Optics for Central Receiver Solar Power Plants, Central Receivers, 1979.

[43] S. Yang, W. Tao, Heat Transfer, fourth ed., High Education Press, Beijing, 2006 (in Chinese).

[44] H. Gao, Statistical Computing, Peiking University Press, Beijing, 1995 (in Chinese).

[45] J.P. Holman, Heat Transfer, ninth ed., McGraw-Hill, New York, 2002.

[46] J. Ballestrín, R. Monterreal, Hybrid heat flux measurement system for solar central receiver evaluation, Energy 29 (2004) 915–924.

[47] Q. Shun, M. Hou, F. Jin, Particle Physics and Mechanics, Science Press, Beijing, 2011 (in Chinese).

[48] Y.-X. Dong, Z.-P. Song, S.-J. Cui, Perspectives on the measurement of angle of repose, J. China Pharm. Univ. 39 (2008) 317–320 (in Chinese).

[49] S. Chu, J. Dong, S. Wang, J. Wan, H. Zhou, Repose angle of non-adhesive granular materials on a plane, Phys. Exp. 39 (2019) 7 (in Chinese).